Tribocorrosion Dependence on Porosity of TiNi Alloys in Phosphate-Buffered Saline Solution

Latifa Kahloul[1] · Soumaya Meddah[2] · Nasser Eddine Beliardouh[3] · Alex Montagne[4] · Mohamed Bououdina[5] · Said Boudebane[6]

Abstract

Degradations of implants during their service life lead to rejection because of corrosion and wear-related problems, i.e., toxic ions and wear particles released into the human body. In this case, tribocorrosion tests are appropriate ways to investigate the synergistic effect of the corrosion and wear phenomena, on the material implant in simulated body fluids. This study aims to analyze the bio-tribology as well as the tribocorrosion performances of porous TiNi alloys, fabricated from elemental powder mixture (Ti, Ni) by powder metallurgy. The effect of the level in porosity, resulting from four (04) different cold pressing, was investigated against alumina ball in phosphate-buffered saline solution (PBS) at 37 °C. SEM/EDS microstructural analyses revealed the presence of various phases with TiNi as the predominant phase. Obtained results showed that the lowest friction coefficient was recorded for the sample with 33% in porosity rate when sliding against an alumina ball in dry conditions. A high tribocorrosion resistance for all the studied TiNi compositions was also observed. Based on the corrosion parameters and the wear rate, the composition with the highest porosity exhibited the optimum performance.

Graphical Abstract

Influence of the porosity rate on the specific wear rate.
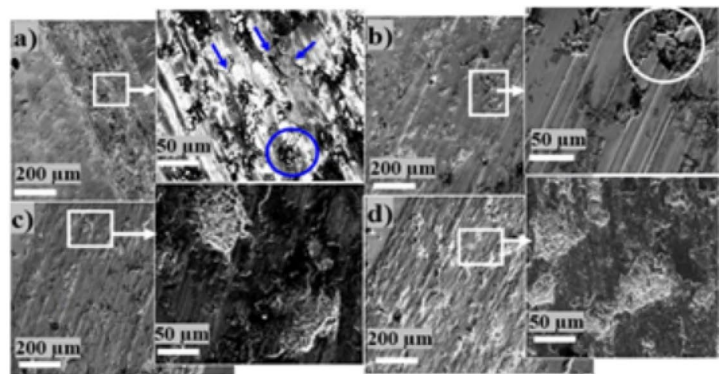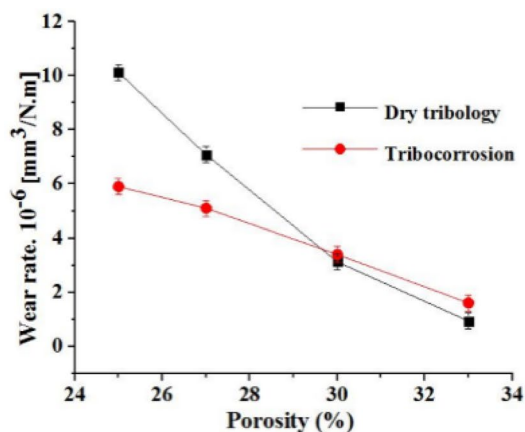
Keywords

1 Introduction

Ti–Ni (50/50) alloys (nearly equal Ti and Ni compositions) have been widely studied in respect of their exceptional properties, including excellent corrosion resistance, high mechanical characteristics, shape memory effect, and

✉ Latifa Kahloul
latifabiomat@gmail.com

Extended author information available on the last page of the article

biocompatibility [1–3]. Specifically, diverse biomedical applications emerged such as fixation plates of the bone fracture, orthodontic wires, staples, and correction rods of the spine [4]. Moreover, these alloys exhibit high wear resistance due to cyclic hardening and pseudo-plastic deformation [5, 6]. Zhang et al. studied the sliding wear behavior of a super-elastic Ti–Ni alloy; the obtained results showed a resistance ten (10) times higher than that of a pure Ti and Ni, respectively [7]. Rabin et al. attributed the increase in resistance to indentation and wear of the TiNi alloy to the Young's modulus/hardness (E/H) ratio [8]. Another study showed that the mechanism of the alternative sliding wear can be associated to abrasion, adhesion, and delamination [9]. The wear resistance of this alloy was found to be conditioned by the precipitation of Ti_3Ni_4 phase and by the thermal characteristics of the martensitic transformation [10].

The porous form of Ti–Ni alloys has also been utilized in the biomedical field because of the supplementary properties, such as low density, high toughness, relatively low stiffness, and a Young's modulus very similar to that of human bone [10–12]. Alternatively, open porosities can alter the bone growth by cell migration and, thus, improve the fixation at the interface bone/implant [13, 14]. Yong-Hua et al. analyzed the influence of the porosity on the corrosion characteristics of a porous Ti–Ni alloy in a physiological medium. The obtained results indicated that the corrosion resistance decreased with increase in porosity rate [15, 16]. However, no agreement regarding the tribological performances of the porous Ni–Ti alloy has been reached. Wu et al. studied the wear properties of a shape memory Ni–Ti alloy for orthopedic implants with different porosities. It was found that porosity, phase transformation temperature, and annealing temperature are the major factors influencing the wear characteristics of the porous Ni–Ti alloy [17]. Meanwhile, another work reported that low porosity leads to better wear resistance, which was attributed to the super elasticity [18]. Therefore, the influence of the porosity on wear behavior was not well defined as reported in numerous studies. Nevertheless, some studies reported the beneficial effect of porosity and suggested that, it can help absorb the impact energy that accompanies cracks. Besides, porosity can act as lubricant reservoir under wet sliding conditions, which is a considerable advantage in the wear process. Porosity improves the roughness of materials' surface, reduces the area of contact between two rubbing surfaces, and consequently promote the detachment of particles during sliding as reported in the literature [19].

In the field of prostheses biocompatibility, it is important to highlight that the release of metal ions and wear particles in fluids and tissues of human/animal body [11] are the major problems that challenges scientific research so far. Among the proposed strategies used to solve this problem, this is to minimize, at the extreme limits, the wear rate parameter [20]. In this context, this research work aims to investigate the effect of porosity on the tribocorrosion performances of porous Ti–Ni alloys elaborated by powder metallurgy process under varying pressure before sintering.

2 Experimental Procedures

2.1 Samples Elaboration

Porous Ti–Ni alloys were prepared by the solid-phase-sintering process from elementary Ti (99.9% of purity and an average particle size ~ 100 µm) and Ni powders (99.8% of purity and 25 µm in size). The 50/50 at.% powder mixture was milled for 2 h using a ball mixer then subjected to cold compaction in a tungsten carbide (WC) matrix under different pressures (221, 295, 369, and 443 MPa). The purpose of varying the compaction pressure was to obtain samples with different porosities. The dimensions of obtained spherical-shaped tablets are 13 mm in diameter and 5 mm in thickness. Subsequently, the as-obtained tablets were sintered at 950 °C for 7 h in a tube furnace under a flow argon atmosphere. The experimental procedure flow chart is depicted in Fig. 1.

Figure 2 displays SEM images of porous Ti–Ni alloys. It can be observed that (i) four main crystalline phases compose the microstructure, i.e., Ti-rich phase, TiNi, Ti_2Ni, and $TiNi_3$ (Fig. 2a), which are in good agreement with the literature [21]; (ii) a number of pores (regardless of size) are distributed over the surface of the entire samples which decreases as the compaction pressure increases. In addition, all samples display interconnected pores with different and complex shapes (Fig. 2a–d) while spheroidization of pores is only observed in the sample compacted at 443 MPa (Fig. 2d). The adopted fabrication method and the microstructural characteristics presented in Table 1 (phase composition and porosity) of the different specimens have been described in detail in previous study [21].

The data reported in Table 1 reveal a close chemical composition (Ti and Ni) of both samples X_1 and X_3, but the porosity percentage is quite different. The level of the applied pressure (P) during cold-pressing agglomeration step is the main factor that influences the final microstructure of TiNi powder alloys; i.e., higher P leads to less porosity and vice versa but there will be no influence on size distribution and shape of pores as reported in the literature [21].

2.2 Dry Tribological Tests

The tribological tests were carried out using an oscillating tribometer TRIBO tester. All tests were conducted under conventional ball-and-disk configuration with alumina ball (13 GPa) as a static partner, at ambient temperature and about 40% of relative humidity. The tribological test

Fig. 1 SEM micrographs of the fabricated specimens cold compacted under different pressures of **a** 221 MPa where (1 represents Ti rich, 2-Ti$_2$Ni, 3-TiNi, and 4-TiNi$_3$), **b** 295 MPa, **c** 369 MPa, and **d** 443 MPa
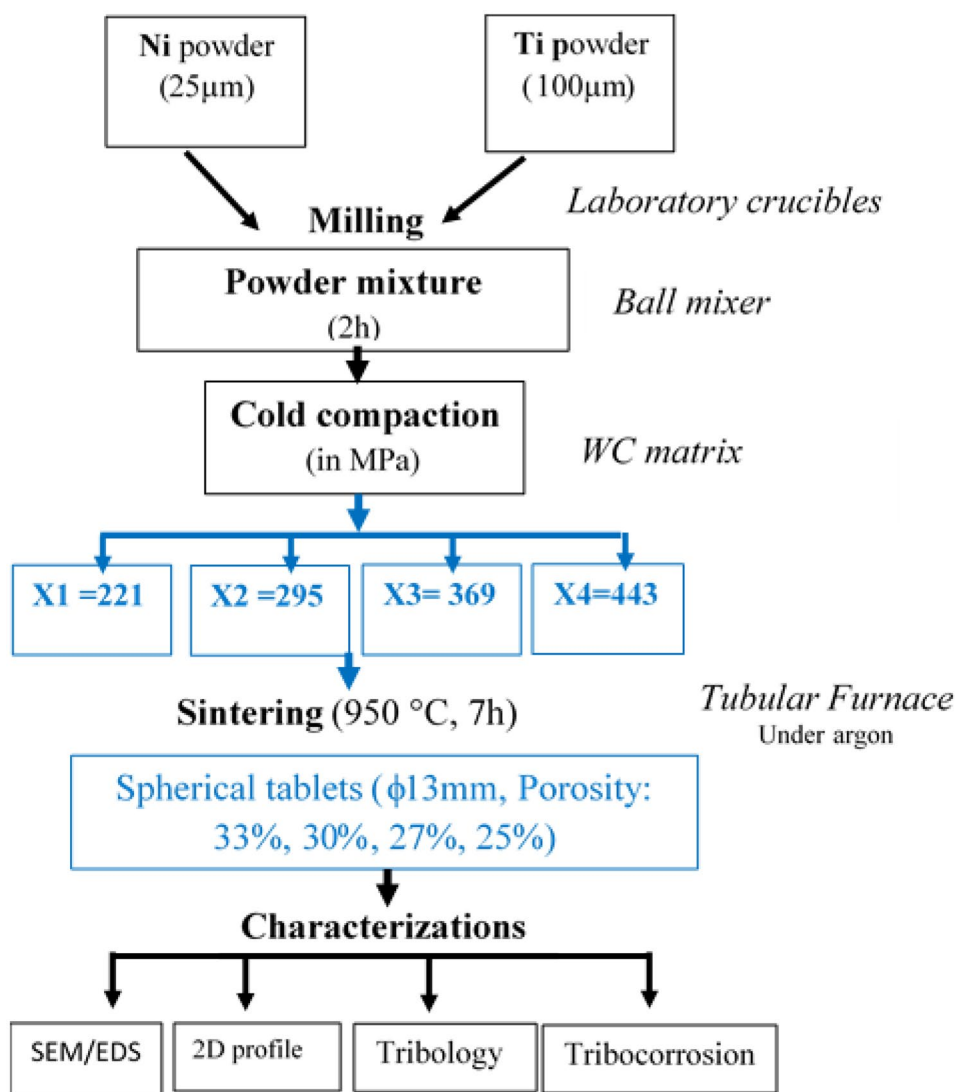
parameters (10 mm/s of sliding speed, 20 m in total sliding distance, and 5 N of applied load) are kept constant for all the specimens. Prior to the test, the sample was gradually polished SiC papers until No. 1200, rinsed in distilled water, ultrasonically cleaned in acetone bath and then air-dried.

2.3 Tribocorrosion Tests

Tribocorrosion tests were performed by means of a three-electrode cell made of Teflon with the sample as the working electrode, a platinum wire as the counter-electrode, and Ag/AgCl as a reference electrode. The experiments were carried out in phosphate-buffered saline solution (PBS) which includes (in g/l) NaCl = 8, KCl = 0.2, Na$_2$HPO$_4$ = 1.15, and KH$_2$PO$_4$ = 0.2 [22] at ambient temperature. The same tribological parameters (applied load, sliding speed, and total sliding distance) as for dry tribological tests were adopted.

The electrochemical tests were performed using a Potentiostat/Galvanostat *Solatron Analytical 1285A*. The potentiodynamic polarization curves during sliding were plotted in the potential range between −0.6 and +0.8 V with a scanning speed of 1 mV/s. All the experiments were duplicated.

Polarization resistance (R_p) was determined from linear polarization measurements as the slope of the linear region of the Potential vs. Current curve, near corrosion potential (E_{corr}). The corrosion parameters [E_{corr}, anodic (β_a), and cathodic (β_c) slopes] were estimated from the Tafel extrapolation method. The corrosion current density I_{corr} was also calculated based on one form of the classical Stern–Geary equation (Eq. 1).

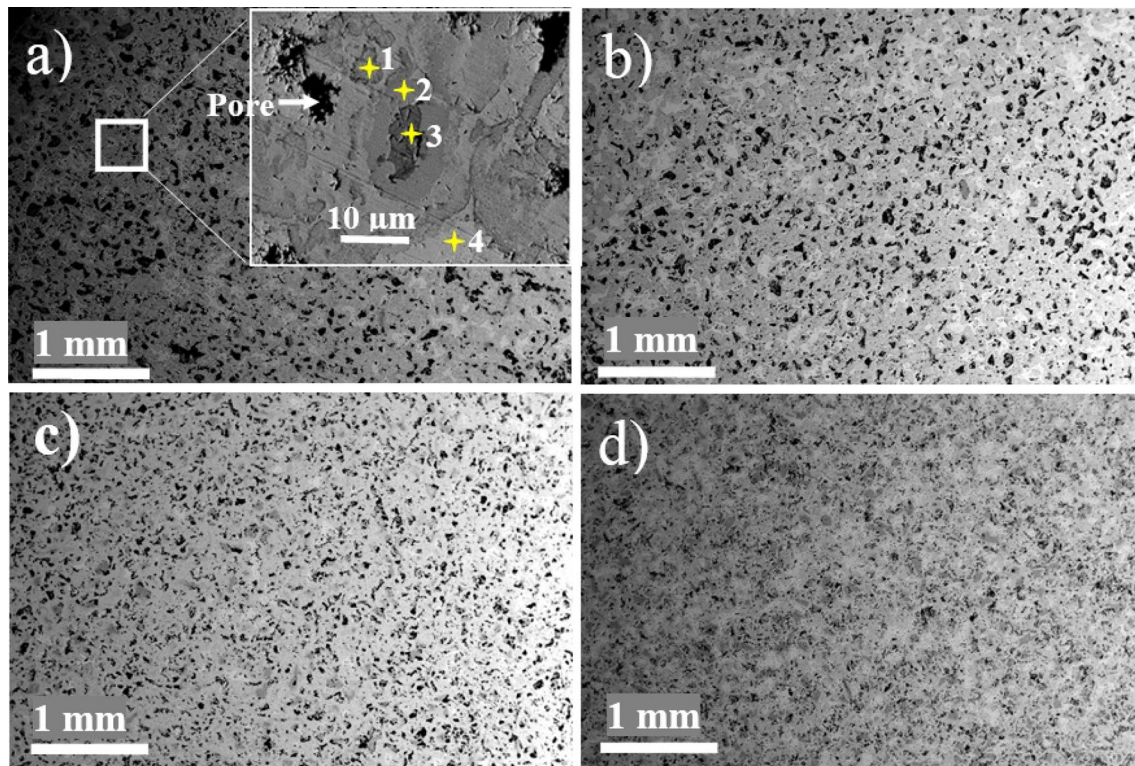$$\frac{1}{R_p} = 2.3\left(\frac{\beta_a + |\beta_c|}{\beta_a|\beta_c|}\right)I_{corr}. \tag{1}$$

Fig. 2 Experimental procedure flow chart

Table 1 Chemical composition of the fabricated TiNi alloys

Specimen	Pressure (MPa)	Porosity (%)	Ti (wt%)	Ni (wt%)
X_1	221	33	52.24	47.76
X_2	295	30	48.65	51.35
X_3	369	27	52.43	47.57
X_4	443	25	53.41	46.59

2.4 Surface Characterization

The surface and the chemical composition of the specimens before and after tribo-tests were analyzed by scanning electron microscope (*ZEISS-EVO/MA25*) coupled with energy dispersive spectroscopy (*OXFORD Instruments X-MaxN*).

The specific wear rate (W_s) was calculated based on the Archard law equation [23]:

$$W_s = \frac{V}{PL},\tag{2}$$

where V is the wear volume loss (mm^3), P is the applied load (N), and L is the sliding distance (m). The wear volume (V) was estimated from the 2D profile of the wear track using an optical profilometer type *Veeco Wyko N19300*.

3 Results and Discussion

3.1 Tribological Behavior

The dry-sliding conditions have been selected as a means to accelerate the wear process. Since the purpose was to assess the relative wear resistance of the porous TiNi specimens, dry-sliding test against ceramic ball was considered as extreme aggressive conditions. Therefore, such data are required, in the optic to evaluate the material performances, and in order to get a clearer idea about degradation mechanisms before tests in vivo.

Figure 3 illustrates the evolution of the coefficient of friction (COF) as a function of the sliding time of the tested samples in dry conditions. Overall, the representative curves shown in Fig. 3 manifest the same trend characterized by two distinct stages. In all cases, the COF starts at low values (0.16) corresponding to the first contact of alumina ball asperities against specimen's surface. The running-in period is the first step, clearly shown in X_1 and X_3 cases. X_1 samples exhibited the larger one. After that, the COF increases drastically reaching an optimum value of ~ 0.7, as a consequence of an increase in frictional forces, probably due to abrasion wear and maintaining a steady state. The average values of the COF are 0.417 and 0.6 for X_1 and X_3, respectively. Very short running-in periods are observed for X_2 and X_4 samples.
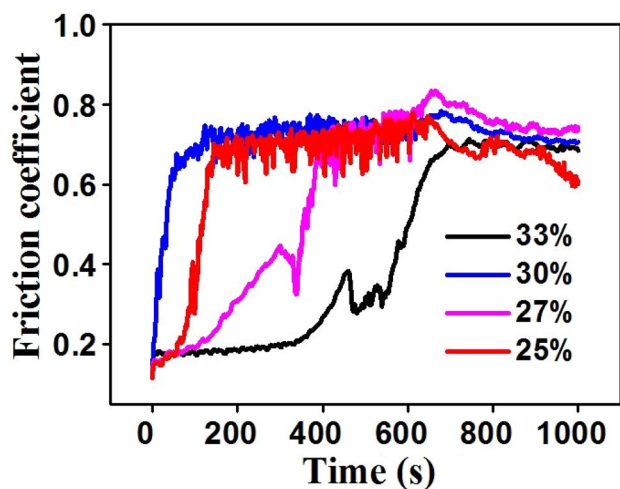
Fig. 3 The COF evolution vs. sliding time of the TiNi specimens, at different level in porosity (porosity rate) in dry conditions
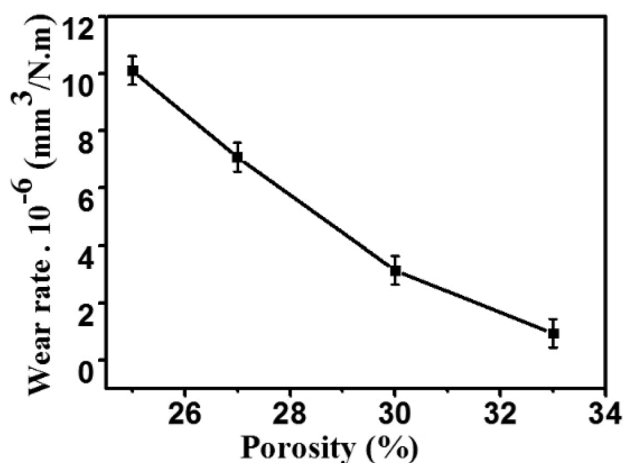

Fig. 4 Influence of the total porosity on the specific wear rate

The first stage corresponds to an accommodation of the two surfaces when rubbing against one another. Alumina ball has a higher hardness, thus the relief (roughness) of the tested specimens was reduced by plastic deformation. The second stage begins when the COF acquires stability. The average values of the COF are 0.59 and 0.64 for X_2 and X_4, respectively.

As observed, an increase in the specimen porosity leads to a decrease in the average COF at the steady state, because voids (pores) facilitate plastic deformations of the superficial layers in direct contact with the static partner. Finally, the evolution of COF as a function of the sliding time indicates that the porosity rate level has direct influence on the friction and wear regime of TiNi porous materials.

Figure 4 depicts the wear rate (W_s) estimation based on the volume loss calculation of the tested samples. It can be

seen that the value of W_s decreases with increase in the total porosity percentage. The positive influence (W_s reduction) of the total porosity is remarkable in the studied range between 20 and 35%; therefore, the interdependence "COF-Ws" has been established.

3.2 Wear Mechanisms Analysis

Figure 5 shows wear tracks of the tested specimens. Scratches and grooves parallel to the sliding direction are common features for all the samples (Fig. 5a–d). It is evident that specimens have undergone abrasive wear. Small cracks can be detected on the worn surface joining two adjacent pores as indicated by blue arrows (Fig. 5a). One can also observe wear particles entrapped in pores, as highlighted in circles in Fig. 5a, b. The latter indicates a fatigue rupture of the top layers and wear debris formation, respectively. Particles of wear debris are produced by breaking of the asperities, removed from disk specimens and/or created by tribochemical layer formation (oxidation during rubbing of the opponent pairstatic partner) wiche becomes brittle, then transformed into debris after several sliding cycles against alumina ball. It is important to mention that wear debris can play the role of a third body wear and consequently contribute to plowing specimen surfaces.

Moreover, the worn surfaces of X_3 and X_4 specimens, having lesser total porosity (25% and 27% in Fig. 5c, d), indicate another aspect of wear tracks. In addition to the scratched marks, signs of delamination wear are also observed. Higher magnification SEM micrographs reveal that the wear track of TiNi disk exhibits specific regions (indicated by yellow arrows) suggesting delamination of the tribo-layer in largest-flake type debris. Finally, under the conditions of the tests conducted against alumina balls, higher porosity (30% and 33%) results in an abrasive wear while lower porosity (25% and 27%) manifests a delamination wear in addition to an abrasive wear.

3.3 Tribocorrosion Behavior

Figure 6 illustrates the tribocorrosion results obtained simultaneously under the conditions adopted in this study. Figure 6a shows the evolution of COF of the samples recorded during the tribocorrosion tests. It can be noticed that the curves have a similar appearance to those obtained under dry test conditions, i.e., characterized by two stages. One can see that the PBS solution does not play any lubrication role; it only diminishes friction forces. The average values of the COF are smaller. Figure 6a is marked by the presence of a fluctuation in each curve and that this trend exists in all friction curves regardless the total porosity rate in TiNi materials. X_3 and X_4 manifest the lowest mean friction coefficient ~ 0.4 compared to ~ 0.46 for X_1 and X_2. The
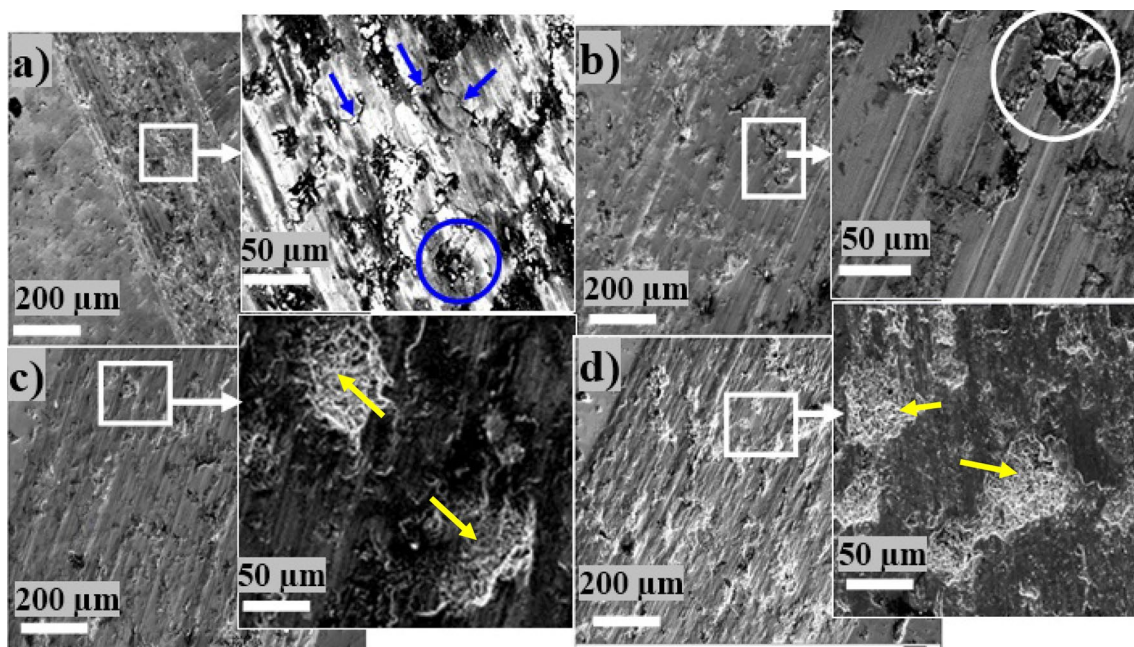
Fig. 5 Wear tracks analysis after tribo-tests of **a** X_1, **b** X_2, **c** X_3, and **d** X_4
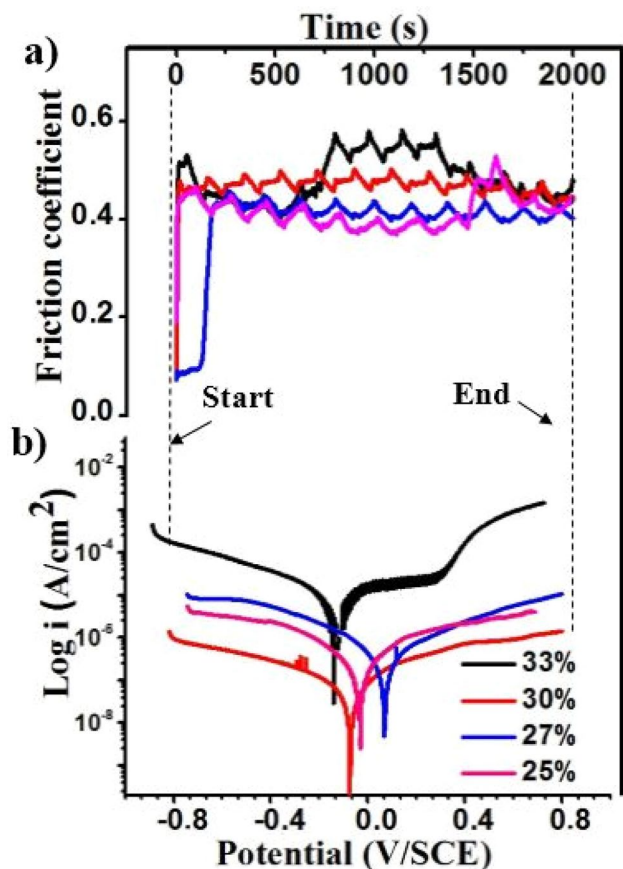

Fig. 6 Tribocorrosion tests results **a** coefficient of friction as function of time, **b** potentiodynamic polarization curves (Tafel plots)

COF fluctuates along the periods around 180–190 s upon the sliding time in all cases. This phenomenon can be related to the most probable main mechanisms: (i) the formation of wear debris, which persists in the contact area during a certain period resulting in the rise of the COF, followed by the elimination of these debris through the flow of the electrolyte inducing a decrease of the COF. (ii) The presence of pores that conditions the efficiency and stability of the passive film, i.e., the formation and rupture of an unstable Ti oxide layer.

Figure 6b illustrates the potentiodynamic polarization measurements in PBS solution. The variation in the porosity level of studied samples may cause some difficulties to quantify precisely the corrosion current density (I_{corr}). The exact estimation of the surface in contact with the electrolyte is not conceivable, since the I_{corr} value depends upon it. However, the evaluation of the electrochemical performance was possible by means of comparison of the evolution of the corrosion parameters. Overall, one can note that all the curves depicted in Fig. 6b present the same trend. They are characterized by the presence of a wide constant current plateau in the anodic region, which means that samples spontaneously passivate in this condition (i.e., formation of a thin oxide passive layer on the external surface). The main electrochemical parameters of the investigated specimens calculated based on the Tafel curves are presented in Table 2 (all the presented potentials are relative to the Ag/AgCl value).

Considering the E_{corr} parameter, the most electropositive value was demonstrated by the X_3

Table 2 Electrochemical parameters from tribocorrosion tests at 37 °C in phosphate-buffered saline solution

Specimen	β_a (mV dec.$^{-1}$)	β_c (mV dec.$^{-1}$)	I_{Corr} 10^{-7} (A/cm^2)	E_{Corr} (V)	R_p (kΩ cm^2)
X_1	235.42	185.66	58.1	− 0.13	7.756
X_2	792.02	202.06	2.79	− 0.072	884.74
X_3	731.84	511.55	7.61	0.068	171.93
X_4	361.07	352.04	3.11	− 0.034	249.00

specimen ($E_{corr} = + 0.068$ V) closely followed by X_2 ($E_{corr} = − 0.072$ V), which presents also the smallest value of corrosion current density ($I_{corr} = 2.79$ 10^{-7} A/cm^2). Besides, when taking into account the polarization resistance, the highest value was observed in the case of X_2 ($R_p = 885$ kΩ).

The X_1 sample (black curve) presents the largest horizontal plateau, with a pitting potential $E_{pp} = 300$ mV and a $\Delta E = 431$ mV calculated from of the formula $\Delta E = E_{pp} − E_{Corr}$. This confirms the tendency for sample X_1 to passivate. Moreover, the presence of the fluctuations associated with the sliding on the curve of the X_1 sample is attributed to the damage of the passive film by the mechanical action. However, the curves of samples X_2, X_3, and X_4 do not show a pitting in the anodic range.

Finally, in the same tested conditions conducted during tribocorrosion process, the X_2 specimen shows the highest (best) electrochemical performances. This is may be due to the homogeneous distribution of the porosity.

3.4 Quantification of Wear After Tribocorrosion Tests

The quantitative interpretation of the tribocorrosion phenomena takes into consideration, both the degradation due to the corrosion and the mechanical wear. The total volume loss of the synergistic effect (V_t) parameter can be used to appreciate the resistance against tribocorrosion:

$$V_t = V_m + V_c, \tag{3}$$

where V_m and V_c are the volume loss due to the mechanical wear and the electrochemical corrosion, respectively. According to the Stack criteria, the (V_c/V_m) ratio is an established approach to determine the predominant mechanism of degradation in the contact zone. Therefore, the following possibilities may exist [24]:

- $V_c/V_m < 0.1$: the degradation takes place by mechanical wear.
- $< V_c/V_m < 1$: the mechanical effect is dominant; the degradation is controlled by wear-corrosion.
- $< V_c/V_m < 10$: the chemical effect is dominant; the degradation is controlled by corrosion-wear.

- $10 < V_c/V_m$: the degradation takes place only by corrosion.

The determination of the V_m is established by the analysis of the geometry of wear traces (Eq. 2) while V_c is calculated using Faraday's law [25] (Eq. 4):

$$V_c = \frac{I_p M t}{n F \rho}, \tag{4}$$

where I_p is the passivation current density; M is the atomic mass; t is the time; n is the charge number for the oxidation reaction ($n = 2$); F is the Faraday number (96,500); and ρ is the density.

Based on the above criteria, it is found that the calculated (V_c/V_m) is < 0.1. Besides, previous work reported that the passive film formed on the surface consists of two layers for all the specimens [21]. This will improve the electrochemical behavior of the porous Ti–Ni alloys during tribocorrosion processes. Therefore, only the deterioration by mechanical wear has to be taken into consideration when estimating the specific wear rate W_s after the tribocorrosion tests.

Figure 7 depicts the variation of the wear rate obtained after the tribocorrosion tests, based only on V_m (Eq. 2). It can be noticed that the same trend already obtained for dry sliding is observed; i.e., the wear rate decreases with the increase in the porosity level. However, it shall be noted that the values obtained at lower porosity rates (25% and 27%) are in the same order as for W_s under dry conditions, while for the high porosity rate (30% and 33%), the obtained values represent half as for dry conditions (divided by factor 2). This result confirms the role of trapping the porosity of loose particles by reducing the abrasive wear in the contact area [24]. In addition, the good tribological properties of titanium oxide (TiO$_2$) formed during immersion in the electrolyte, have already been demonstrated in previous studies [26, 27].

3.5 Tribocorrosion Mechanisms Analysis

Figure 8 displays the tribocorrosion results in terms of the synergistic effect of both the rubbing against alumina ball (mechanical wear) and the chemical attack by aggressive ions in the Phosphate-Buffered Saline Solution (corrosion).
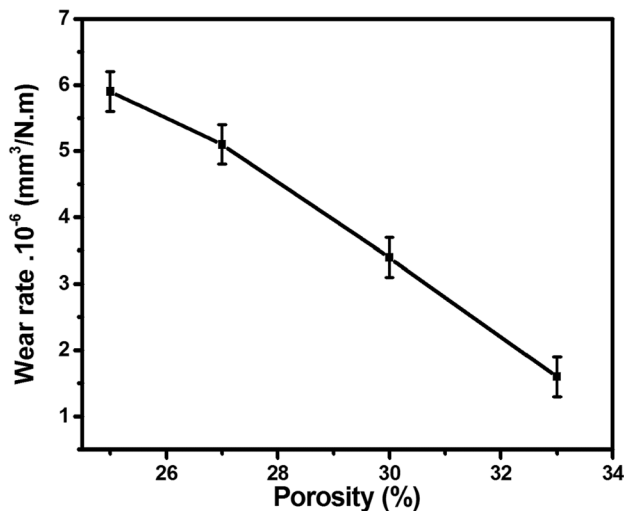
Fig. 7 Evolution of wear rate as function of the porosity of TiNi alloys

The two degradation mechanisms do not proceed separately but mainly proceed concurrently.

The analysis of wear mechanisms, evolving in the tribocorrosion system in this study, indicates that all the specimens manifest the same trends regarding the surface degradation. SEM micrographs of X_1 (highest porosity level), X_3 (middle level), and X_4 (lowest level) are presented in Fig. 8a–c. The worn zones reveal the presence of plastic deformation areas, particles embedded in pores, and scratches oriented along the sliding direction. It is noticed also that all the wear tracks are free of oxides and no delamination zones can be found, indicating the absence of oxidative and delamination wear mechanisms during the tribocorrosion tests. However, the three worn surfaces show different aspects in morphology. The microstructural component Ti-rich phase (Fig. 1) remains in X_1 specimen (Fig. 8a; yellow circle) while it disappears totally from surfaces, leaving voids (Fig. 8b, c) after its transformation into wear debris. Consequently, the high porosity rate results in the lowest wear rate (Fig. 7), and therefore, enhances the resistance against tribocorrosion.

Finally, the mechanisms of degradation evolving during tribocorrosion are essentially plastic deformations and micro-abrasion wear, meanwhile the porosity rate plays a positive effect on the tribocorrosion resistance.

3.6 Discussion

In this study, the mechanical degradation effect is considered as the major parameter in the estimation of the tribocorrosion wear rate. It is supposed that no chemical dissolution phenomenon takes place, e.g., no galvanic effect,

oxide-reduction, etc. Only rubbing under constant load, against alumina is responsible for the surface degradation of specimen. Therefore, the interpretation of the obtained results may be as follows.

During the tribocorrosion process, asperities of alumina balls started scratching the surface of the disk, creating wear debris. After several cycles, two schemas (possibilities) become possible, regardless of the porosity.

The first one (Fig. 8c) is that when the metallic Ti-rich phase, transforms into wear debris leaving voids, and contributed to the increase of the wear rate value estimation (W_s) because it depends on volume loss calculation (based on 2D profiles).

The second possible way (Fig. 8a) is that when Ti-phase resists (not removed) and penetrates deeply in the matrix. Therefore, the volume loss estimation (and consequently W_s value) is only relative to the debris formed by the micro-abrasion process.

In fact, as mentioned above, the tribocorrosion process occurs according to the synergistic effect following the occurrence of the dual degradation processes. Therefore, to better understand how the porosity influences the wear rate (W_s), it is necessary to take into account the chemical effect.

Herein, it is established that during the tribocorrosion test, the passive film is continuously being destroyed and re-formed (Fig. 5a). The variation (fluctuation) of COF corresponds to the de-passivation and re-passivation of the alloy. The passive film, most probably TiO_2, processes as a chemical reaction against the electrolyte completely different, compared to that of alloy's surface (mixture of Ti_xNi_y phases). Alternatively, galvanic cells are established during the wear process in the electrolyte, where the bare metal (worn zone) can act as an anode and its edge (the passive layer) acts as a cathode. Therefore, the electrochemical reactions occur non uniformly over the entire surface and somehow can explain the difference in the tribocorrosion behavior of the tested specimens.

On the other hand, the applied pressure during the fabrication process (cold compaction), which ultimately represents the difference between specimens, does not play any role in the tribocorrosion process through the induced residual stresses. Because sintering the sample at 950 °C annihilates all of the residual stresses, so, this factor cannot be considered here.

Finally, it has been deduced that both mechanical and electrochemical mechanisms are responsible for the removal of particles from the alloy during friction. As a result, the plastic flow of the alloy through plowing, particle detachment, and third body formation are found to be directly dependent on the porosity.
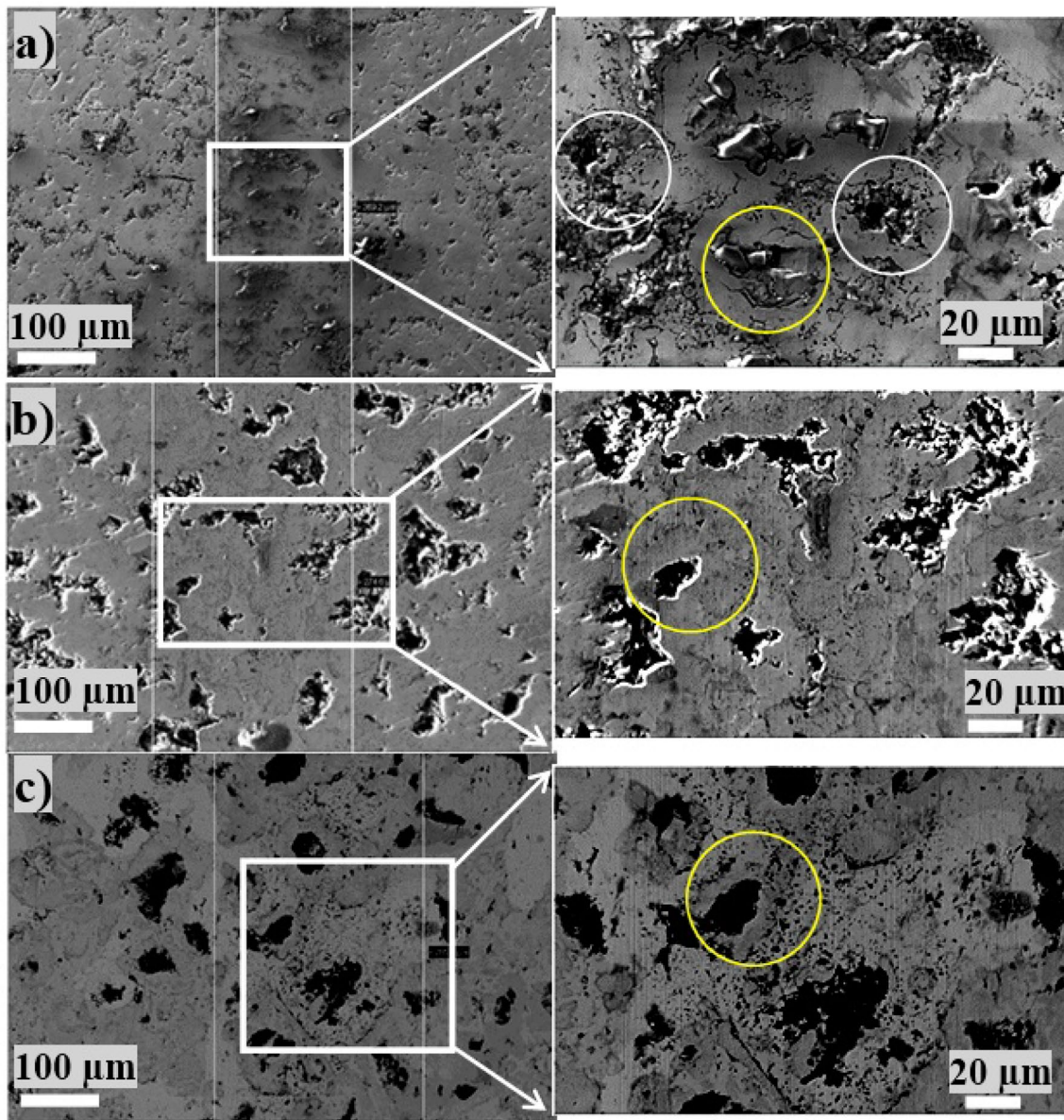
Fig. 8 Wear tracks analysis after tribocorrosion tests of specimens **a** X_1, **b** X_2, and **c** X_3. White circles indicated the initial pores and holes. Voids left by initial Ti-rich phase removal (dissolved) are circled in yellow

4 Conclusion

The tribocorrosion behavior of porous Ti–Ni alloys, with different porosity level obtained by solid phase sintering under different cold compaction pressures, was studied. Based on the results obtained, the following conclusions are drawn:

- The microstructural examinations showed that TiNi-phase is dominant.
- The average friction coefficient in dry-sliding tests decreases with increase in the porosity level.

- Two wear mechanisms were identified in dry conditions, namely abrasive and delamination.
- The formation of the protective oxide film was found to be the main phenomenon that governs the variation of the friction coefficient during tribocorrosion. Furthermore, the wear mechanisms were mainly plastic deformation and micro-abrasion.
- The best resistance against corrosion was demonstrated by X_2 (30% in porosity) specimen based on potentiodynamic polarization curves.

- The tribocorrosion behavior of the studied specimen was mainly related to the porosity and stability of the passive film formed on the surface.

4.1 Future Work

Bacterial infection, corrosion, and wear are the most common causes of the failure of the use of biomedical metallic implants. Therefore, additional work should focus on biocompatibility, i.e., the investigation of the antibacterial activity of the elaborated materials against biofilm-related microbes.

Author Contributions All authors contributed to the study conception and design. Material preparation, data collection, and analysis were performed by Dr. LK, Dr. SM, Pr. AM, and Pr. SB. Pr. NEB and Pr. MB wrote the manuscript. I, the Corresponding Author, declare that the manuscript has been read and approved by all named authors.

Data Availability All data generated or analyzed during this study are included in this published article.

Declarations

Conflict of interest The authors have no relevant financial or non-financial interests to disclose.

References

1. Ting Liu K, Gong Duh J (2008) Grain size effects on the corrosion behavior of $Ni_{50.5}Ti_{49.5}$ and $Ni_{45.6}Ti_{49.3}Al_{5.1}$ films. J Electroanal Chem 618:45–52. https://doi.org/10.1016/j.jelechem.2008.02.020
2. Tang G, Ho JK, Dong G, Hua M (2016) Fabrication self-recovery bulge textures on TiNi shape memory alloy and its tribological properties in lubricated sliding. Tribol Int 6:11–22. https://doi.org/10.1016/j.triboint.2015.12.011
3. Zhao X, Ma L, Yang M, Ding Y, Shen X (2010) Electrochemical properties of Ti–Ni–H powders prepared by milling titanium hydride and nickel. Int J Hydrog Energy 35:3076–3079. https://doi.org/10.1016/j.ijhydene.2009.07.017
4. Hu T, Wen CS, Sun GY, Wu SL, Chu CL, Wu ZW, Li GY, Lu J, Yeung KW, Chu PK (2010) Wear resistance of NiTi alloy after surface mechanical attrition treatment. Surf Coat Technol 205:506–510. https://doi.org/10.1016/j.surfcoat.2010.07.023
5. Clayton P (1993) Tribological behavior of a titanium–nickel alloy. Wear 162–164:202–210. https://doi.org/10.1016/0043-1648(93)90502-D
6. Li DY (1996) Wear behaviour of TiNi shape memory alloys. Scr Mater 34:195–200. https://doi.org/10.1016/1359-6462(95)00515-3
7. Zhang C, Farhat ZN (2009) Sliding wear of superelastic TiNi alloy. Wear 267:394–400. https://doi.org/10.1016/j.wear.2008.12.093
8. Neupane R, Farhat Z (2013) Wear and dent resistance of superelastic TiNi alloy. Wear 301:682–687. https://doi.org/10.1016/j.wear.2012.11.017
9. Neupane R, Farhat Z (2014) Wear mechanisms of nitinol under reciprocating sliding contact. Wear 315:25–30. https://doi.org/10.1016/j.wear.2014.02.018
10. Arciniegas M, Casals J, Manero JM, Pena J, Gil FJ (2008) Study of hardness and wear behaviour of NiTi shape memory alloys. J Alloys Compd 460:213–219. https://doi.org/10.1016/j.jallcom.2007.05.069
11. Bansiddhi A, Sargeant TD, Stupp SI, Dunand DC (2008) Porous NiTi for bone implant. Acta Biomater 4:773–782. https://doi.org/10.1016/j.actbio.2008.02.009
12. Xiong JY, Li YC, Wang XJ, Hodgson PD, Wen CE (2008) Titanium–nickel shape memory alloy foams for bone tissue engineering. J Mech Behav Biomed Mater. https://doi.org/10.1016/j.jmbbm.2007.09.003
13. Li DS, Zhang YP, Ma X, Zhang XP (2009) Space-holder engineered porous NiTi shape memory alloys with improved pore characteristics and mechanical properties. J Alloys Compd 474:1–5. https://doi.org/10.1016/j.jallcom.2008.06.043
14. Bansiddhi A, Dunand DC (2008) Shape-memory NiTi foams produced by replication of NaCl space-holders. Acta Biomater 4:1996–2007. https://doi.org/10.1016/j.actbio.2008.06.005
15. Li Y-H, Rao G-B, Rong L-J, Li Y-Y, Ke W (2003) Effect of pores on corrosion characteristics of porous NiTi alloy in simulated body fluid. Mater Sci Eng A 363:356–359. https://doi.org/10.1016/S0921-5093(03)00629-4
16. Li Y-H, Rao G-B, Rong L-J, Li Y-Y (2002) The influence of porosity on corrosion characteristics of porous NiTi alloy in simulated body fluid. Mater Lett 57:448–451. https://doi.org/10.1016/S0167-577X(02)00809-1
17. Wu S, Liu X, Yeung KW, Xu ZS, Chung CY, Chu PK (2012) Wear properties of porous NiTi orthopedic shape memory Alloy. J Mater Eng Perform 21:2622–2627. https://doi.org/10.1007/s11665-012-0392-z
18. Wu S, Liu X, Wu G, Yeung KW, Zheng D, Chung CY, Xu ZS, Chu PK (2013) Wear mechanism and tribological characteristics of porous NiTi shape memory alloy for bone scaffold. Biomed Mater Res 101:2586–2601. https://doi.org/10.1002/jbm.a.34568
19. AminulIslam M, Farhat ZN (2011) Effect of porosity on dry sliding wear of Al–Si alloys. Tribol Int 44:498–504. https://doi.org/10.1016/j.triboint.2010.12.007
20. Kosec T, Mocnik P, Legat A (2014) The tribocorrosion behaviour of NiTi alloy. Appl Surf Sci 288:727–735. https://doi.org/10.1016/j.apsusc.2013.10.116
21. Kahloul L, Chadli H, Beliardouh NE, Bououdina M (2019) Cold pressing dependence on microstructure and electrochemical performance of porous TiNi alloy. Mater Res Express 6:096559. https://doi.org/10.1088/2053-1591/ab3023
22. Karimi S, Nickchi T, Alfantazi A (2011) Effects of bovine serum albumin on the corrosion behaviour of AISI 316L, Co–28Cr–6Mo, and Ti–6Al–4V alloys in phosphate buffered saline solutions. Corros Sci 53:3262–3272. https://doi.org/10.1016/j.corsci.2011.06.009
23. Sun XT, Kang ZX, Zhangc XL, Jiang HJ, Guan RF, Zhang XP (2011) A comparative, study on the corrosion behavior of porous and dense NiTi shape memory alloys in NaCl solution. Corros Sci 56:6389–6396. https://doi.org/10.1016/j.electacta.2011.05.019

24. Marques ID, Alfaro MF, da Cruz NC, Mesquita MF, Takoudis C, Sukotjo C, Mathew MT, Barão VA (2016) Tribocorrosion behavior of biofunctional titanium oxide films produced by micro-arc oxidation: Synergism and mechanisms. J Mech Behav Biomed Mater 60:8–21. https://doi.org/10.1016/j.jmbbm.2015.12.030

25. Cao S, Maldonado SG, Mischler S (2015) Tribocorrosion of passive metals in the mixed lubrication regime: theoretical model and application to metal-on-metal artificial hip joints. Wear 324–325:55–63. https://doi.org/10.1016/j.wear.2014.12.003

26. Dong H, Bell T (2000) Enhanced wear resistance of titanium surfaces by a new thermal oxidation treatment. Wear 238:131–137. https://doi.org/10.1016/S0043-1648(99)00359-2

27. Siva Rama Krishna D, Brama YL, Sun Y (2007) Thick rutile layer on titanium for tribological applications. Tribol Int 40:329–334. https://doi.org/10.1016/j.triboint.2005.08.004

Authors and Affiliations

Latifa Kahloul[1] · Soumaya Meddah[2] · Nasser Eddine Beliardouh[3] · Alex Montagne[4] · Mohamed Bououdina[5] · Said Boudebane[6]

1 Mines Metallurgy Materials Laboratory L3M, National High School of Mines and Metallurgy Amar LASKRI, Annaba, Algeria

2 Research Center in Industrial Technologies - CRTI, P.O. Box 64, 16014 Cheraga, Algiers, Algeria

3 Laboratoire d'Ingénierie Des Surfaces (LIS), Université Badji Mokhtar, BP12, 23000 Annaba, Algeria

4 Laboratory of Mechanics Surfaces and Processing Materials, ARTS ET METIERS ParisTech, 8, Boulevard Louis XIV, 59046 Lille Cedex, France

5 Department of Physics, College of Science, University of Bahrain, PO Box 32038, Zallaq, Kingdom of Bahrain

6 Laboratory of Metallurgy and Materials Engineering (LMGM), Badji Mokhtar University, 23000 Annaba, Algeria